Journal of Power Sources 215 (2012) 48–52

Contents lists available at SciVerse ScienceDirect

Journal of Power Sources

journal homepage: www.elsevier.com/locate/jpowsour

Short communication

SnO_2 nanospheres supported Pd catalyst with enhanced performance for formic acid oxidation

Haiting Lu [a], Yang Fan [a,*], Ping Huang [b], Dongli Xu [a]

[a] College of Chemistry and Chemical Engineering, Xinyang Normal University, Xinyang 464000, China
[b] Fujian Institute of Research on the Structure of Matter, Chinese Academy of Sciences, Fuzhou 350002, China

HIGHLIGHTS

- SnO_2 nanospheres were employed as support material for Pd catalyst.
- SnO_2 nanospheres process extraordinary promotional effect on Pd catalyst.
- Pd/SnO_2 exhibits enhanced catalytic activity and stability towards FAO.

GRAPHICAL ABSTRACT

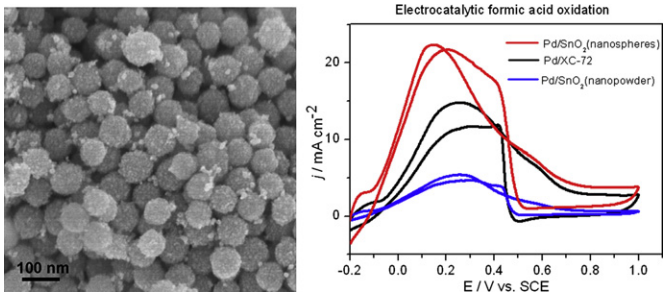

ARTICLE INFO

Article history:
Received 12 March 2012
Received in revised form
28 April 2012
Accepted 1 May 2012
Available online 11 May 2012

Keywords:
Tin dioxide
Nanospheres
Palladium catalyst
Formic acid oxidation

ABSTRACT

SnO_2 nanospheres were employed as the support material for Pd catalyst. The as-prepared Pd/SnO_2 catalyst exhibited remarkably improved electrocatalytic activity and stability towards formic acid oxidation, in comparison with that of the Vulcan XC-72 carbon black and the commercial SnO_2 nanopowder supported Pd catalyst. The enhanced catalytic performance may arise from the unique structure and surface properties of the SnO_2 nanospheres, which process extraordinary promotional effect on Pd catalyst.

1. Introduction

Pd-based electrocatalysts have recently attracted great attention as promising anode catalyst for direct formic acid fuel cells (DFAFCs) [1–6]. In contrast to the commonly used Pt catalysts, Pd catalysts can catalyze the formic acid oxidation (FAO) via a more direct pathway, bypassing the strongly bound CO intermediate [2,3]. Thus, Pd catalysts are much less prone to CO poisoning and deactivation than that of Pt catalysts. However, to fulfill the demand of higher power output in working DFAFCs, the catalytic activity and durability the Pd-based catalysts still need to be substantially improved [3]. The development of advanced support materials has been demonstrated to be a promising way to improve the activity and stability of fuel cell electrocatalysts, including the Pd catalysts for FAO [7–11]. Recently, transition metal oxides based materials, such as TiO_2, CeO_2 and SnO_2, have shown attractive properties in applications of electrocatalyst support materials [12–14]. Compared to the commonly used carbon support, these alternative support materials usually have good CO tolerance and corrosion resistance [7]. In particular, the SnO_2 based supports have exhibited remarkable promotional effects on the Pt catalysts by reducing CO-

* Corresponding author. Tel./fax: +86 376 6391825.
E-mail address: yfanchem@163.com (Y. Fan).

0378-7753/$ – see front matter © 2012 Elsevier B.V. All rights reserved.
doi:10.1016/j.jpowsour.2012.05.003

poisoning and modifying electronic properties of Pt [15]. To date, however, the metal oxide supported Pd catalysts for formic acid oxidation have been rarely explored [16,17].

In this study, we report the synthesis of Pd catalyst supported on the SnO_2 nanospheres. The results demonstrate that the presence of SnO_2 nanospheres can significantly enhance the activity and stability of Pd catalyst towards FAO, as compared to that of the Vulcan XC-72 carbon black and commercial SnO_2 nanopowder.

2. Experimental

2.1. Reagents and apparatus

$K_2SnO_3 \cdot 3H_2O$ (99.9%), glucose (99%) and Na_2PdCl_4 (Pd 36.4%) were purchased from Aladdin Chemistry Co., Ltd. Vulcan XC-72 carbon black was purchased from Cabot Corporation. $NaBH_4$ (98%) were purchased from Sinopharm Chemical Reagent Co., Ltd. Pd/C (20% Pd on carbon, Johnson Matthey) was purchased from Alfa Aesar. Nafion (5 wt.%) was purchased from Sigam-Aldrich. Water used throughout all experiments was purified with the Millipore system.

2.2. Structure characterizations

Scanning electron microscopy (SEM) images were obtained on a Hitachi S-4800 field emission scanning electron microscope. Transmission electron microscopy (TEM), high-resolution TEM (HRTEM), and energy dispersive X-ray (EDX) analyses were preformed using a JEOL JEM-2010 transmission electron microscope. X-ray diffraction (XRD) analyses were carried out with a Bruker D8 Advance X-ray diffractometer with Cu-K*a* radiation ($\lambda = 1.5406$ Å). The metal loading of the Pd catalysts was determined using an inductively coupled plasma–atomic emission spectroscopy (ICP-AES, Optima 2000 DV).

2.3. Electrochemical measurements

All electrochemical experiments were performed with a CHI 850C electrochemical analyzer (CH Instruments, Shanghai, China). A conventional three-electrode system was used for all electrochemical experiments, which consisted of a platinum wire as counter electrode, an standard calomel electrode (SCE) as reference electrode, and a glassy carbon (GC) electrode (3 mm diameter) coated with the catalyst as working electrode. The catalyst ink was prepared by dispersion of the catalyst powder (5 mg) in 1 mL water under ultrasonic treatment to form a homogeneous suspension (5 mg mL^{-1}). Then, 5 μL of the catalyst ink was cast on the freshly polished GC electrode surface and dried under an infrared lamp. Then, 2 μL of dilute Nafion solution (0.02 wt.%) was placed on the surface of the above catalyst modified GC electrode and dried at room temperature. Before measurements, the working electrode was first activated with cyclic voltammetry (0–1.0 V, 50 mV s^{-1}) in an Ar-saturated 0.5 M H_2SO_4 solution until a steady CV was obtained.

CO-stripping experiments were conducted in 0.5 M H_2SO_4 solution, which was purged with Ar for 30 min and then bubbled with high-purity CO gas for 15 min for CO adsorption on catalysts. The residual CO in the solution was subsequently removed by Ar purging for 30 min. The CO-stripping cyclic voltammetry curves were recorded within the potential between −0.2 and 1.0 V at a scan rate of 50 mV s^{-1}.

2.4. Preparation of Pd catalyst

The SnO_2 nanospheres were synthesized by hydrothermal reaction of K_2SnO_3 in an aqueous glucose solution followed by calcination at 400 °C in air [18]. The SnO_2 supported Pd catalyst was prepared through reduction of Na_2PdCl_4 with $NaBH_4$. In a typical procedure, 50 mg of SnO_2 was dispersed in 50 mL of water by sonication. Then, 2 mL of Na_2PdCl_4 solution (0.06 mM) was added, and the mixture was stirred for 1 h. A freshly prepared 10 mL of $NaBH_4$ solution (0.1 M) was added to the solution at 0 °C, followed by stirring at room temperature overnight. Finally, it was filtered, washed with water and ethanol, and vacuum-dried at 70 °C for 6 h. The as-prepared product was denoted as Pd/SnO_2–S. For comparison, the commercial SnO_2 nanopowder and Vulcan XC-72 carbon black supported Pd catalyst with same Pd loading was prepared by the above procedure, which were denoted as Pd/SnO_2–P and Pd/XC-72, respectively.

3. Results and discussion

The XRD patterns of the Pd/SnO_2–S catalyst in Fig. 1 show the coexistence of Pd and SnO_2 crystalline. The diffraction peaks at $2\theta = 39.4°$, 46.2°, 66.3° and 80.6° are indexed as the (111), (200), (220), and (311) planes of Pd, respectively, indicating that Pd forms the typical face-centered cubic (*fcc*) crystal structure [5]. The other diffraction peaks at 2θ value of 26.5, 33.8, 51.3 and 54.3 are attributed to the (110), (101), (211) and (220) planes the tetragonal rutile structure of SnO_2 support, respectively [18]. The energy dispersive X-ray (EDX) spectroscopy shows the peaks corresponding to Sn, O, and Pd, with the C and Cu peaks emanating from the TEM grid (Fig. S1). The SEM and TEM images for the Pd/SnO_2–S catalyst are shown in Fig. 2. It is clear to see that a number of perfect nanospheres with the size ranging from 80 nm to 90 nm are evenly distributed. The TEM image in Fig. 2c further reveals that the SnO_2 nanospheres were constructed from primary nanoparticle building blocks with a mean size of *ca.* 9 nm. The deposition of Pd nanoparticles (NPs) on the SnO_2 supports is visualized with HRTEM (Fig. 2d). It can be seen that these nanoparticles have good crystallinity with well-defined fringes. The 0.33 nm lattice spacing is assigned to the (110) plane of rutile SnO_2 crystalline. The lattice fringes with a *d* spacing of 0.23 nm correspond to the (111) plane of face-centered cubic Pd, indicating that the Pd NPs grew along the most stable (111) crystal planes on the SnO_2 surfaces.

Fig. 3 depicts the cyclic voltammograms (CVs) of different catalysts-coated electrodes in Ar-saturated 0.5 M H_2SO_4 solution. The CV profiles show the characteristics of polycrystalline palladium in the hydrogen adsorption–desorption region (−0.2 to 0.1 V), double-layer capacitance region (0.15–0.3 V) and metal oxidation–reduction region (above 0.3 V). Two pairs of well-

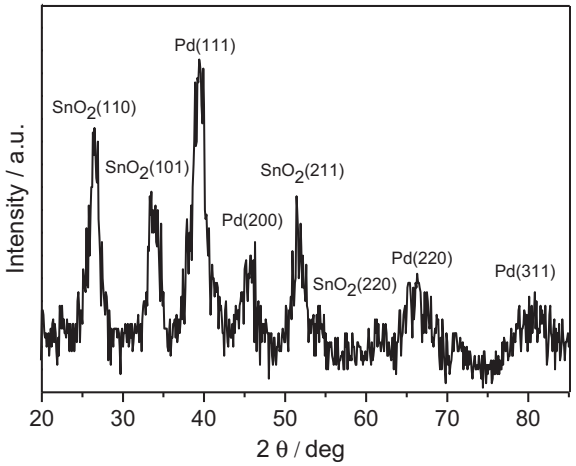

Fig. 1. XRD patterns of the Pd/SnO_2–S catalyst.

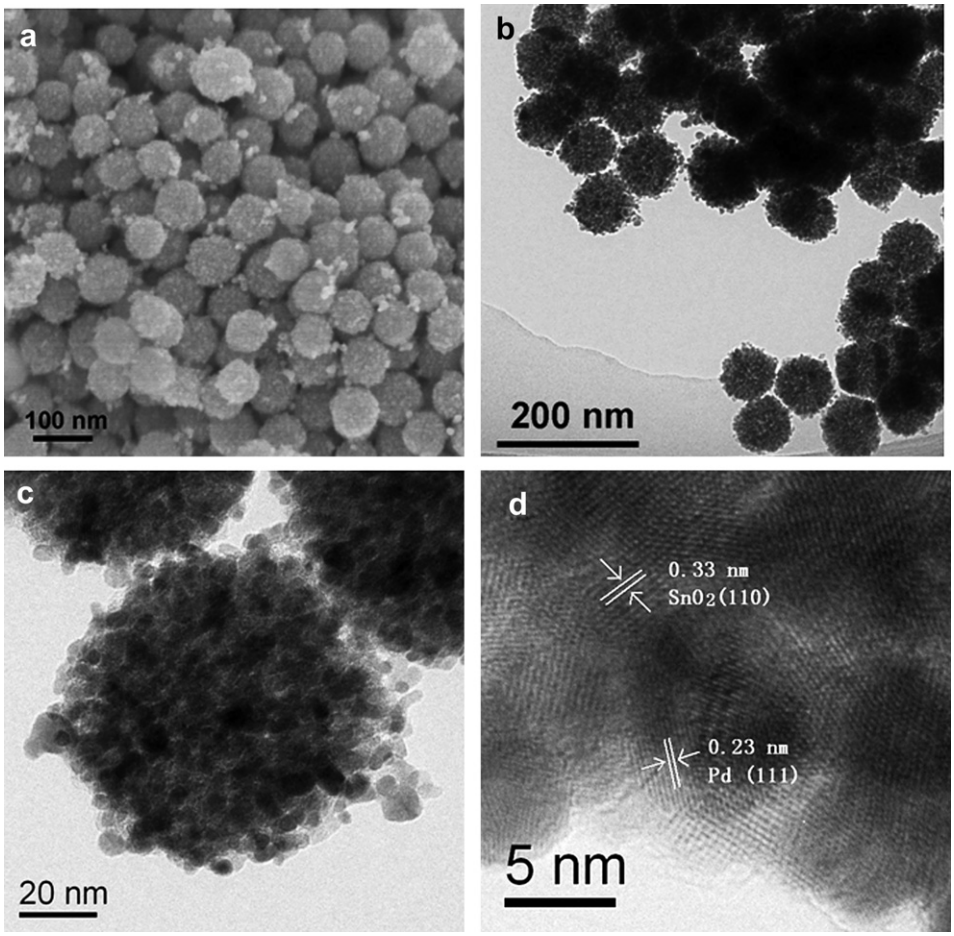

Fig. 2. SEM (a), TEM (b and c) and HRTEM (d) images of the Pd/SnO_2–S catalyst.

defined current peaks corresponding the hydrogen adsorption and desorption were observed for all the Pd catalysts. At potentials more negative than −0.1 V in the cathodic scan, the Pd/SnO_2–S catalyst exhibited a sharp increase in current due to the hydrogen evolution. The enlarged hydrogen adsorption peak of the Pd/SnO_2–S catalyst indicates that it has larger surface area. CO-stripping voltammetry was performed to get a more accurate electrochemically active surface area (ECSA) of the Pd catalysts (Fig. 4). The ECSA was estimated by integrating the voltammograms corresponding to the CO-stripping peak by assuming a charge of 420 μC cm^{-2} for electro-oxidation of the CO monolayer on the catalyst surfaces [19]. It found that the ECSA value of Pd/SnO_2–S (79.5 m^2 g^{-1}) was larger than those of Pd/SnO_2–P (35.6 m^2 g^{-1}) and Pd/XC-72 (69.3 m^2 g^{-1}), indicating that more active sites are available at the Pd/SnO_2–S catalyst [20]. It is noteworthy that the reduction peak potential of Pd oxide shifted positively at the Pd/SnO_2–S catalyst (0.45 V), relative to those at the Pd/SnO_2–P catalyst (0.43 V) and Pt/XC-72 catalyst (0.42 V). This positive shift of the Pd oxide reduction potential has also been observed in some other Pd-based electrocatalysts, which suggests that the metal oxide layer is more readily reduced and hence can activate the electrocatalytic reaction [21].

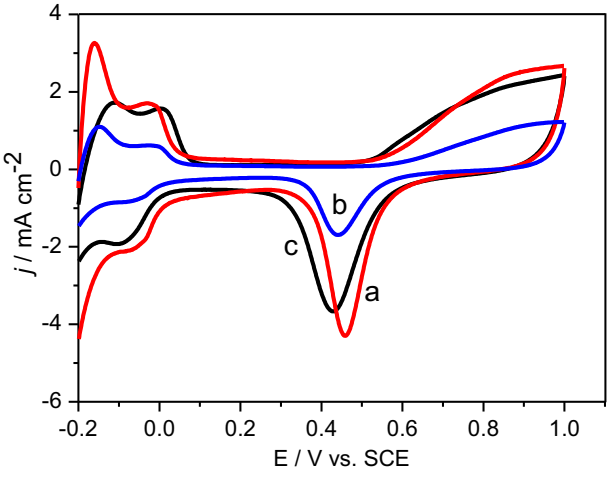

Fig. 3. CVs of the Pd/SnO_2–S (a), Pd/SnO_2–P (b) and Pd/XC-72 (c) catalysts in an Ar-saturated 0.5 M H_2SO_4 solution at a scan rate of 50 mV s^{-1}.

The catalytic performance of the Pd catalysts toward formic acid oxidation was investigated in 0.5 M H_2SO_4 solution containing 0.5 M HCOOH. As shown in Fig. 5, the first oxidation peak observed on Pd/SnO_2–S at 0.14 V in the positive scan is assigned to the oxidation of HCOOH. The minor hump at about 0.55 V is due to the Pd oxidation, which leads to the decrease in activity and drop of the oxidation current. In the negative scan, due to the Pd oxide formation, the oxidation of formic acid starts only after the reduction of metal oxide layer. It can be seen that the catalyst surface is regenerated with the removal of Pd oxide at around 0.5 V, resulting in a sudden jump in current of formic acid oxidation. The peak potential for FAO at the Pd/SnO_2–S catalyst was negatively

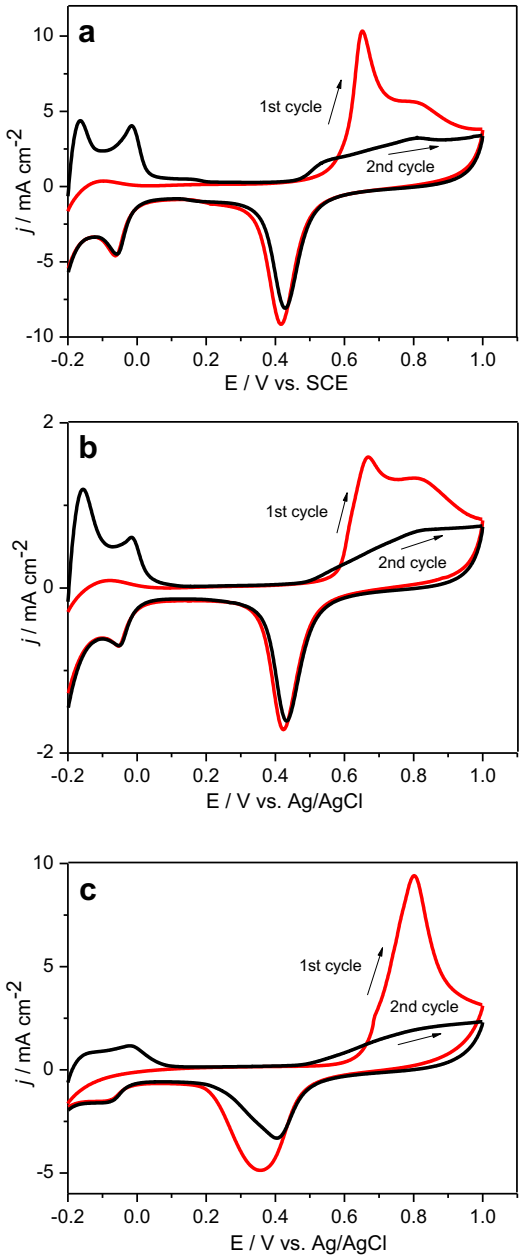

Fig. 4. CO-stripping voltammograms of the Pd/SnO_2–S (a), Pd/SnO_2–P (b) and Pd/XC-72 (c) catalysts in 0.5 M H_2SO_4 solution at a scan rate of 50 mV s^{-1}.

shifted by *ca.* 100 mV as compared to those of the Pd/SnO_2–P catalyst (0.24 V) and Pd/XC-72 catalyst (0.26 V), indicating substantially decreased overpotential at the Pd/SnO_2–S catalyst. Moreover, the onset potential for FAO at the Pd/SnO_2–S catalyst located at *ca.* −0.12 V, that is more negative those of the Pd/SnO_2–P (−0.10 V) catalyst and Pd/C (−0.07 V). The peak current density for FAO at the Pd/SnO_2–S catalyst was 22.3 $mAcm^{-2}$, which was about 4.2 times that of the Pd/SnO_2–P catalyst (5.3 $mAcm^{-2}$) and 1.5 times that of the Pd/XC-72 catalyst (14.3 $mAcm^{-2}$), respectively. Therefore, the Pd/SnO_2–S catalyst exhibited enhanced catalytic activity for formic acid oxidation in terms of the oxidation peak potential, peak current density and onset potential. In addition, the superior catalytic activity of the Pd/SnO_2–S catalyst to that of the commercial Pt/C (JM) catalyst was also illustrated in Fig. S2. The mass current density for FAO at the Pd/SnO_2–S catalyst was also

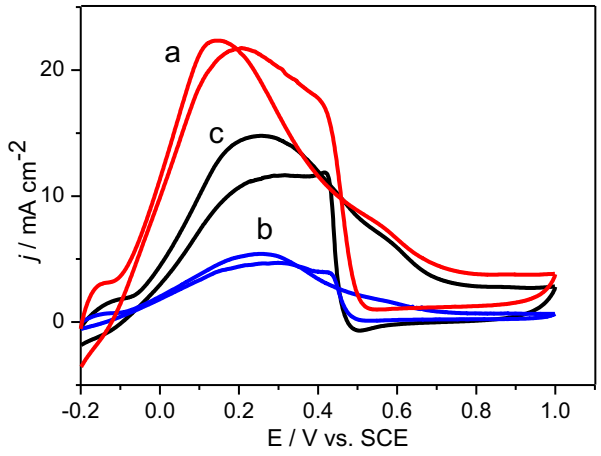

Fig. 5. CVs of the Pd/SnO_2–S (a), Pd/SnO_2–P (b) and Pd/XC-72 (c) catalysts in an Ar-saturated 0.5 M H_2SO_4 solution containing 0.5 M formic acid at a scan rate of 50 mV s^{-1}.

remarkably increased as compared to those of the other two catalysts (Fig. S3). Since all the Pd catalysts were synthesized by the same procedure in aqueous solution using $NaBH_4$ as reducing agent, the SnO_2 nanospheres support must play a vital role in catalytic activity enhancement of the Pd catalysts. The unique morphology of the SnO_2 nanospheres may allow a homogeneous distribution of Pd NPs, and most of the active phases are available at the surface of nanospheres, which resulted in a maximum usage of the Pd catalysts. However, for the Pd/XC-72 catalyst, the commercial Vulcan XC-72 carbon black usually contains considerable amount of micropores, which could limit the access of reactant molecules to the inner electrocatalytic sites.

CO-stripping experiments were carried out to further investigate the promotional effect of the SnO_2 support material. As shown in the CO-stripping voltammograms (Fig. 4), the hydrogen desorption peaks were completely suppressed in the lower potential region, which is due to the saturated coverage of CO_{ads} species on the Pd sites. After the complete oxidation of the CO_{ads} species via the first cycle of CV scan, the Pd sites in the catalysts were refreshed and the hydrogen adsorption peak was regenerated. As discussed above, the Pd/SnO_2–S catalyst exhibited a larger CO-stripping peak and the corresponding ECSA value than those of the Pd/XC-72 and Pd/SnO_2–P. The most notable difference between CO-stripping at the SnO_2 supported Pd catalysts and the carbon black supported Pd catalyst is the negative shift of the CO-stripping peak in the former. At the Pd/XC-72 catalyst, the oxidation peak of CO_{ads} located at 0.8 V. In contract, the CO_{ads} oxidation peak appeared at 0.65 and 0.67 V on the Pd/SnO_2–S and the Pd/SnO_2–P, respectively. As known, the lower potential for CO oxidation indicates the higher CO-poisoning tolerance of the catalysts. This result suggests that the poisoning effect of CO was largely decreased due to the presence of SnO_2 support material, which is helpful to weakening the adsorption strength of CO on Pd sites. Moreover, the onset potential of CO oxidation also shifted negatively for the two SnO_2 support Pd catalysts (ca. 0.47 V), with respect to that of the Pd/C catalyst (0.58 V). This result can be interpreted by the formation of OH_{ads} species on SnO_2 surface at lower potentials, which activate the CO_{ads} oxidation through a bifunctional mechanism [15].

The long-term stability and durability of the Pd catalysts were further investigated by chronoamperometry tests (Fig. 6 and Fig. S4). The Pd/SnO_2–S catalyst exhibited a higher initial current density compared to the other catalysts, because of the presence of a larger number of catalytic active sites available for FAO. Although

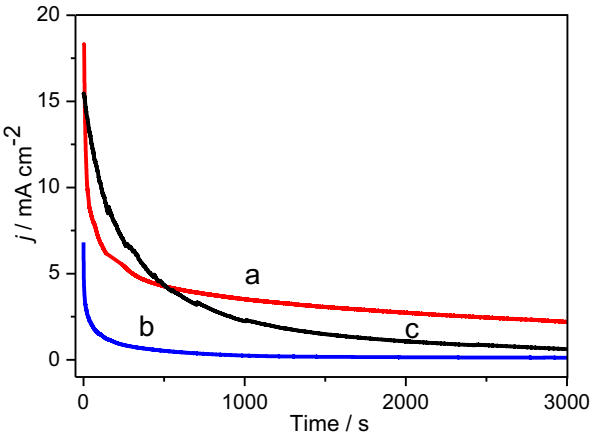

Fig. 6. Chronoamperometric curves of the Pd/SnO_2–S (a), Pd/SnO_2–P (b) and Pd/XC-72 (c) catalysts recorded at 0.2 V in an Ar-saturated 0.5 M H_2SO_4 solution containing 0.5 M formic acid.

the oxidation current on Pd/SnO_2–S dropped quickly at the beginning, it stabilized much faster and remained higher than that of Pd/XC-72 after 500 s. This may be ascribed to the stability of nanospheres structure which is less vulnerable to dissolution, Ostwald ripening, and aggregation than the amorphous carbon black and SnO_2 nanopowder under the reaction conditions. The final current density at the Pd/SnO_2–S catalyst after holding the cell potential at 0.2 V for 3000 s was 2.1 $mAcm^{-2}$, which is much higher than that of the Pd/XC-72 catalyst (0.64 $mAcm^{-2}$), the Pd/SnO_2–P catalyst (0.20 $mAcm^{-2}$) and the commercial Pd/C (JM) catalyst (0.41 $mAcm^{-2}$). The stability of the Pd/SnO_2–S catalyst can be attributed the SnO_2 nanospheres support, which alleviates the poisoning of strongly bound CO_{ads} intermediates, and hence improves the catalytic activity and the stability [15].

4. Conclusions

In summary, the Pd catalyst consisting Pd NPs supported on the SnO_2 nanospheres was prepared via a simple aqueous phase method. As compared with the Vulcan XC-72 carbon black and the SnO_2 nanopowder, we have observed both improved electrocatalytic activity and stability for the SnO_2 nanospheres supported Pd catalysts. The enhanced catalytic performance can be mainly ascribed to the unique structure and surface properties of the SnO_2 nanospheres. This work has opened up new opportunities for the development of metal oxides supported fuel cell electrocatalysts.

Acknowledgements

This work was financially supported by the National Natural Science Foundation of China (No. 21002082), the Key Project of Chinese Ministry of Education (No. 210129) and the Science and Technology Key Project of Henan Education Department (No. 12A150020).

Appendix A. Supplementary material

Supplementary data associated with this article can be found in the online version at doi:10.1016/j.jpowsour.2012.05.003.

References

[1] Y. Zhu, Z. Khan, R.I. Masel, J. Power Sources 139 (2005) 15.
[2] E. Antolini, Energy Environ. Sci. 2 (2009) 915.
[3] X. Yu, P.G. Pickup, J. Power Sources 182 (2008) 124.
[4] V. Mazumder, S. Sun, J. Am. Chem. Soc. 131 (2009) 4588.
[5] N. Cheng, H. Lv, W. Wang, S. Mu, M. Pan, F. Marken, J. Power Sources 195 (2010) 7246.
[6] H. Meng, C. Wang, P.K. Shen, G. Wu, Energy Environ. Sci. 4 (2011) 1522.
[7] S. Sharma, B.G. Pollet, J. Power Sources 208 (2012) 96.
[8] L. Feng, X. Sun, C. Liu, W. Xing, Chem. Commun. 48 (2012) 419.
[9] X. Chen, G. Wu, J. Chen, X. Chen, Z. Xie, X. Wang, J. Am. Chem. Soc. 133 (2011) 3693.
[10] R.D. Morgan, A. Salehi-khojin, R.I. Masel, J. Phys. Chem. C 115 (2011) 19413.
[11] J. Yang, C. Tian, L. Wang, H. Fu, J. Mater. Chem. 21 (2011) 3384.
[12] S.Y. Huang, P. Ganesan, S. Park, B.N. Popov, J. Am. Chem. Soc. 131 (2009) 13898.
[13] Y.Y. Chu, Z.B. Wang, Z.Z. Jiang, D.M. Gu, G.P. Yin, Adv. Mater. 23 (2011) 3100.
[14] H. Zhang, C. Hu, X. He, L. Hong, G. Du, Y. Zhang, J. Power Sources 196 (2011) 4499.
[15] E. Antolini, E.R. Gonzalez, Catal. Today 160 (2011) 28.
[16] W.L. Qu, Z.B. Wang, Z.Z. Jiang, D.M. Gu, G.P. Yin, RSC Adv. 2 (2012) 344.
[17] B. Xie, Y. Xiong, R. Chen, J. Chen, P. Cai, Catal. Commun. 6 (2005) 699.
[18] X.W. Lou, J.S. Chen, P. Chen, L.A. Archer, Chem. Mater. 21 (2009) 2868.
[19] J.Y. Wang, Y.Y. Kang, H. Yang, W.B. Cai, J. Phys. Chem. C 113 (2009) 8366.
[20] B. Seger, P.V. Kamat, J. Phys. Chem. C 113 (2009) 7990.
[21] S. Guo, S. Dong, E. Wang, Energy Environ. Sci. 3 (2010) 1307.